



Effect of photonic crystal film as support on enhancement of graphite-carbon nitride quantum dots sensitized Bi_2MoO_6 photocatalytic activity

Ruizhen Liu^{1,2} · Qing Wang¹ · Ping Li^{1,3} · Huaiyuan Jiang^{1,3} · Binglin Mai¹ · Liuyong Zhao¹ · Zhiqi Zhang¹ · Yutian Fan^{1,3} · Jian Cheng¹ · Renliang Lyu^{1,3}

Received: 5 July 2022 / Accepted: 5 November 2022 / Published online: 19 December 2022
© The Author(s), under exclusive licence to Springer Science+Business Media, LLC, part of Springer Nature 2022

Abstract

Photonic crystals (PCs) with slow photon effect and multiple scattering for its three-dimensional ordered structure have been applied to improve light utilization and enhance photocatalytic activity. A ternary-structured photocatalyst was prepared. Bi_2MoO_6 was first sensitized by graphite-carbon nitride quantum dots (g-CNQDs) by in situ coupling via a hydrothermal method. The best performance of $\text{Bi}_2\text{MoO}_6/\text{g-CNQDs}$ was 3.56 times higher than that of Bi_2MoO_6 . The introduction of g-CNQDs improved both the light absorption range and charge transfer efficiency for $\text{Bi}_2\text{MoO}_6/\text{g-CNQDs}$ composites. Furthermore, because of the combination of the g-CNQDs with the Bi_2MoO_6 nanosheets, the separation efficiency of photogenerated carriers was improved and the recombination rate was greatly reduced. To further improve light utilization, SiO_2 PCs were composited to the above $\text{Bi}_2\text{MoO}_6/\text{g-CNQDs}$ by spin coating to obtain ternary-structured $\text{Bi}_2\text{MoO}_6/\text{g-CNQDs}/\text{SiO}_2$ PCs. The effect of the photonic band gap (PBG) of PCs on photocatalytic activity was investigated, and the photocatalytic activity was highest when the PBG was located near the absorption peak of g-CNQDs at 464 nm, which was 5.56 times higher than that of pure Bi_2MoO_6 . The farther the photonic PBG is away from the absorption edge of g-CNQDs, the lower the photocatalytic activity of the composite membranes. This work provides a way to construct multiple-structured photocatalysts with high photocatalytic activity and confirms that PCs with precisely tuned band gap will substantially enhance the activity of photocatalysts.

✉ Ping Li
pingli@wit.edu.cn

✉ Renliang Lyu
lyurenliang@wit.edu.cn

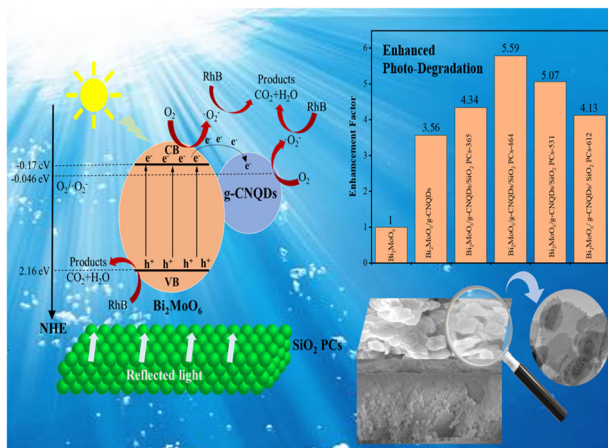
¹ Key Laboratory for Green Chemical Engineering process of Ministry of Education, Key Laboratory of Novel Reactor and

Green Chemical Technology of Hubei Province, School of Chemical Engineering and Pharmacy, Wuhan Institute of Technology, Wuhan, Hubei 430205, China

² Engineering Research Center of Phosphorus Resource Development and Utilization of Ministry of Education, Wuhan, Hubei 430205, China

³ Hubei Three Gorges Laboratory, Yichang, Hubei 443000, China

Graphical abstract



Keywords Pollutant degradation · Graphitic carbon nitride quantum dots · Bi₂MoO₆ Nanosheets · SiO₂ photonic crystals · Ternary structure

Highlights

- A ternary-structured photocatalyst Bi₂MoO₆/g-CNQDs/SiO₂ PCs was synthesized.
- Light harvesting is enhanced and the separation efficiency of photogenerated carriers is improved.
- The optimized Bi₂MoO₆/g-CNQDs/SiO₂ PCs exhibit excellent photodegradation efficiency.
- As-prepared composite film photocatalyst has excellent reproducibility and stability.

1 Introduction

Organic pollutants in water sources around the world are on the rise with the increase of population and the continuous development of industry and agriculture [1–4]. Semiconductor photocatalysis is a promising technology to degrade pollutants by solar energy, which is of great interest due to its low cost, environmental friendliness, high degradation efficiency, and good stability [5–7]. However, the practical application of conventional photocatalysts such as TiO₂ [8], ZnO [9], and WO₃ [10] is still challenging either due to the narrow light absorption range, or due to low charge separation efficiency [11]. Therefore, it is necessary to explore new photocatalytic materials with desirable properties in visible light.

In recent years, Bi-based semiconductor materials such as Bi₂O₃ [12], Bi₂WO₆ [13], BiOBr [14] and Bi₂MoO₆ [15], have become a hot topic of research in photocatalysis. Among them, Bi₂MoO₆ was considered as a promising photocatalyst for visible light degradation of pollutants, because it possesses a suitable band gap of about 2.3–2.8 eV and a typical Orivelis structure consisting of alternating layers of chalcogenide (A_{m-1}B_mO_{3m+1}) and bismuth oxide (Bi₂O₂)²⁺. This type of structure allows Bi₂MoO₆ to exhibit beneficial charge separation [16, 17]. Shimodaira and colleagues first reported Bi₂MoO₆ as a visible light

photocatalyst for O₂ release in 2006 [18]. Then Zhou [19] investigated the photodegradation of pollutants on Bi₂MoO₆. However, the light absorption of pure Bi₂MoO₆ is mainly concentrated in the UV region, which accounts for a small fraction of the solar energy. In addition, the relatively high combination rate of photogenerated electron/hole pairs hinders its wide application. Up to now, there have been a number of studies on the modification of Bi₂MoO₆ [20, 21], among which element doping is an effective strategy for the improvement of photocatalytic properties, especially carbon doping [22]. Recently, doping with quantum dots to improve the photocatalytic performance of Bi₂MoO₆ has received extensive attention due to its quantum confinement effect, high dispersion, large absorption coefficient, ultra-small particle size, with examples including CQDs/Bi₂MoO₆ [23] and CdS QDs/Bi₂MoO₆ [24]. In addition, the construction of heterojunctions is an effective way not only to increase the photoresponse range but also to inhibit the recombination of photogenerated electron-hole pairs, such as Bi₂MoO₆/TiO₂ [25], Bi₂MoO₆/BiOX (X = Cl, Br) [26, 27], Bi₂MoO₆/g-C₃N₄ [28, 29] and Bi₂MoO₆/Bi₂S₃ [30] and other composite catalysts [31, 32]. However, it remains a challenge to realize practical applications of Bi₂MoO₆ by improving the photocatalytic activity.

Graphitic nitrogen carbide (g-C₃N₄) is an emerging semiconductor polymeric material. Due to its stable photocatalytic performance, visible light response, simple

preparation method, relatively narrow band gap ($\sim 2.7\text{eV}$), and high stability, it is widely used in photocatalytic hydrogen production and photocatalytic degradation of organic pollutants [33, 34]. Compared with bulk $g\text{-C}_3\text{N}_4$, graphite nitrogen carbide quantum dots ($g\text{-CNQDs}$) not only have good solubility, but also have superior optical properties, strong fluorescence and upconversion behavior due to quantum confinement and edge effects [35–38]. In contrast to other quantum dots, $g\text{-CNQDs}$ have good stability, low cytotoxicity, excellent biocompatibility, and the ability to convert near-infrared light to visible light, thus facilitating solar energy harvesting. This makes them good candidates to replace conventional quantum dots as attractive candidates for visible light-driven photocatalysis. Chen [39] prepared nanohybrid $g\text{-CNQDs}/\text{Bi}_2\text{MoO}_6$ by in situ coupling. The prepared nanohybrids showed nearly 3- and 6-times higher photocurrent intensity than pure $g\text{-CNQDs}$ and Bi_2MoO_6 , and the photoactivity was significantly increased. The findings suggest that the modification of $g\text{-CNQDs}$ can accelerate charge transfer and improve the light trapping utilization, thus greatly improving the photocatalytic activity of the semiconductor. Nevertheless, the light harvesting efficiency of $\text{Bi}_2\text{MoO}_6/g\text{-CNQDs}$ needs to go one step further.

The introduction of photonic crystals (PCs) into photocatalytic systems has been shown to be a promising approach to enhance the light harvesting efficiency of photocatalysts through the slow photon effect and photonic band gap (PBG) effect of PCs. In addition, the larger specific surface area of PCs contributes to higher absorption capacity of pollutants on the photocatalyst, resulting in improved photocatalytic activity [40, 41]. Based on the unique optical properties of PCs, there have been many studies on the application of PC structures to photocatalytic reactions. There are two main types: one is to prepare semiconductor photocatalysts directly into photonic crystal structures [42–44], such as (N-F)- TiO_2 inverse opals [45]; the other is to prepare photonic crystal films as carriers to support photocatalysts [46, 47], such as $n\text{-TiO}_2/\text{SiO}_2$ opal composite photocatalytic [48] and $\text{CdS QDs}/\text{SiO}_2$ opal thin-film photocatalyst [49]. Experimental results show that both methods can greatly improve photocatalytic efficiency by the synergistic effects of the PCs photonic effect and other chemical effects.

Herein, a composite photocatalyst ($\text{Bi}_2\text{MoO}_6/g\text{-CNQDs}$) supported by SiO_2 PCs was fabricated in order to study the synergistic effect of SiO_2 PCs and $g\text{-CNQDs}$ on improving the photocatalytic activity of Bi_2MoO_6 . Due to the sensitization of $g\text{-CNQDs}$, the light absorption can be effectively extended to visible light, and the complexation of photo-generated carriers can be suppressed. In addition, the band gap of SiO_2 PCs can be flexibly adjusted to enhance light harvesting, which in turn substantially enhances the photocatalytic activity of the semiconductor photocatalyst.

2 Experimental section

2.1 Materials

Urea ($\text{CH}_4\text{N}_2\text{O}$), bismuth nitrate pentahydrate ($\text{Bi}(\text{NO}_3)_3 \cdot 5\text{H}_2\text{O}$), sodium molybdate dihydrate ($\text{Na}_2\text{MoO}_4 \cdot 2\text{H}_2\text{O}$), nitric acid (HNO_3), ethanol ($\text{C}_2\text{H}_5\text{OH}$), ammonia ($\text{NH}_3 \cdot \text{H}_2\text{O}$), methanol (CH_3OH) and sulfuric acid (H_2SO_4) were purchased from Sinopharm Group Co., Ltd. All reagents were of analytical grade and were used without further purification. Deionized water was used throughout all the experiments.

2.2 Synthesis of the Bi_2MoO_6 nanosheets

Bi_2MoO_6 nanosheets were prepared by a one-step hydrothermal method. Firstly, 0.97 g of $\text{Bi}(\text{NO}_3)_3 \cdot 5\text{H}_2\text{O}$ and 0.194 g of $\text{Na}_2\text{MoO}_4 \cdot 2\text{H}_2\text{O}$ were simultaneously added to 80 mL of distilled water, and ultrasonically stirred until uniformly dispersed. Then, 40 mL of ethanol was added under vigorous stirring and stirred for 30 min. Finally, the resulting solution was transferred to a reactor lined with polytetrafluoroethylene and reacted at 180°C for 6 hours. After that, the solution was cooled down to room temperature and washed well with deionized water and ethanol three times. The product was dried in a drying oven at 60°C for 12 h, and then, Bi_2MoO_6 nanosheets were ground and sealed before further use.

2.3 Synthesis of the $g\text{-CNQDs}$ and $\text{Bi}_2\text{MoO}_6/g\text{-CNQDs}$

The $g\text{-CNQDs}$ were prepared according to a reported procedure [50]. Firstly, bulk $g\text{-C}_3\text{N}_4$ was synthesized by calcination of urea at 500°C with a heating rate of 2°C min^{-1} for 3 h in a muffle furnace. Then $g\text{-CNQDs}$ solids were obtained by etching bulk $g\text{-C}_3\text{N}_4$ with concentrated (oxidizing) nitric acid under reflux to cut monolayer or multilayer $g\text{-C}_3\text{N}_4$ into nanoparticles by hydrothermal treatment. $\text{Bi}_2\text{MoO}_6/g\text{-CNQDs}$ were prepared by in situ coupling of $g\text{-CNQDs}$ with Bi_2MoO_6 by hydrothermal method. The required amount of $g\text{-CNQDs}$ powder was added to 40 mL of ethanol and stirred to obtain a uniformly dispersed suspension, then transferred to a hydrothermal reactor and reacted at 180°C for 6 h. After washing and drying, $\text{Bi}_2\text{MoO}_6/g\text{-CNQDs}$ were obtained.

2.4 Synthesis of SiO_2 PCs and the $\text{Bi}_2\text{MoO}_6/g\text{-CNQDs}/\text{SiO}_2$ PCs composite films

PCs were assembled by the room-temperature floatation method [51]. The SiO_2 microspheres were dispersed in an aqueous ethanol solution with a volume ratio of 2:1 to get a 30 wt% SiO_2 suspension. The slides were soaked and

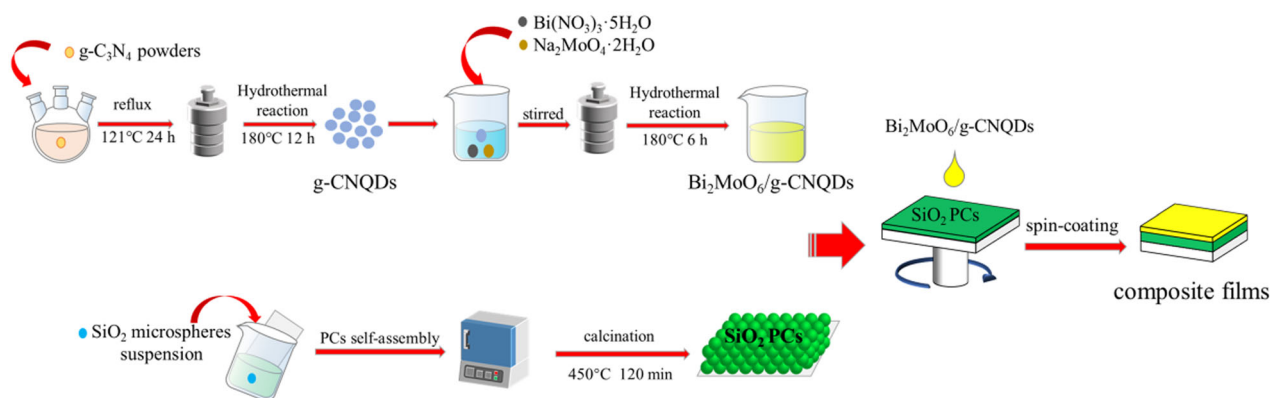


Fig. 1 Schematic diagram of synthesis process for $\text{Bi}_2\text{MoO}_6/\text{g-CNQDs}/\text{SiO}_2$ PCs composite films

rinsed with concentrated Piranha solution containing sulfuric acid and hydrogen peroxide before use, which can replace surface sodium ions with hydrogen ions and greatly reduce the effect of sodium ion diffusion. The slide was then contacted with the surface of the suspension at an angle, and then slowly withdrawn and placed on the table with the suspension-stained side facing up. With the evaporation of the solvent, the SiO_2 microspheres are gradually ordered and self-assembled on the glass substrate to form an opal film. After natural drying, the glass slides carrying the photonic crystal films were placed in a muffle furnace for calcination at 450°C for 120 min to obtain PCs.

The $\text{Bi}_2\text{MoO}_6/\text{g-CNQDs}/\text{SiO}_2$ PCs composite films were prepared by spin coating. $\text{Bi}_2\text{MoO}_6/\text{g-CNQDs}$ were prepared according to the method in 2.3 above. The mixed solution after reaction was transferred from the hydrothermal reactor to the beaker, then polyethylene glycol (PEG 4000) equivalent to 40% of the mass of composite catalyst was added, and a slurry was obtained by magnetic stirring for 12 h. The prepared PCs were placed horizontally on the stage of the spin coater, and then $\text{Bi}_2\text{MoO}_6/\text{g-CNQDs}$ slurry was spin-coated on the PCs. The spin-coating speed was 500 rpm for 9 s in the low-speed stage and 1500 rpm for 45 s in the high-speed stage. After natural drying, the composite film was calcined in a muffle furnace at 450°C for 2 h to obtain composite photocatalyst/photonic crystal composite films. The whole synthesis process is shown in Fig. 1.

2.5 Characterization

The crystalline structure of the samples was analyzed using an X-ray diffractometry (XRD, Bruker D8 ADVANCE), with $\text{Cu-K}\alpha$ ($\lambda = 1.5418 \text{ \AA}$) X-rays as the radiation source and the 2θ scanning range of 10° – 80° . A field emission scanning electron microscope (FESEM, Zeiss Merlin compact-61-78) and a transmission electron microscope (TEM,

JEM-ARM300F) were used to examine the micro-morphology of samples. N_2 adsorption-desorption isotherm experiments were performed on BET specific surface area analyzers (Anton-Paar Quantachrome), and the surface area and pore size distributions of the prepared samples were calculated by Brunauer-Emmett-Teller (BET) and Barrett-Joyner-Halenda (BJH) methods. The optical absorption properties of the prepared sample powders were determined by UV-Vis diffuse reflectance spectrometer (UV-Vis DRS, UV-3600 PLUS) and BaSO_4 as a blank control. The scanning range was 200–800 nm, and the absorbance was converted by the Kubelka-Munk method. The photocurrent and electrochemical impedance spectra (EIS) were measured on an electrochemical workstation (CHI-660D) in a standard three-electrode system. Platinum wire electrode, saturated glycerol electrode, and ITO electrode were used as the counter electrode, reference electrode and working electrode, respectively. The electrolyte solution for the photocurrent intensity test was a 0.1 mol L^{-1} Na_2SO_4 solution, and the electrolyte solution for the EIS test was a 0.1 mol L^{-1} mixture of potassium ferricyanide, potassium ferri-cyanide and potassium chloride. Photoluminescence (PL) measurements were conducted on the powders using a fluorescence spectrophotometer (PL-LS55, PerkinElmer) with excitation wavelength of 420 nm at room temperature. The particle size of SiO_2 microspheres was measured by a Malvern Mastersizer 2000 Particle Analyzer (Mastersizer 2000, Malvern). The PCs were scanned by UV-Vis spectrophotometer (UV-1700PC) to study PBG and other properties.

2.6 Photocatalytic performance test

The photocatalytic activity of the synthesized catalyst was evaluated by the photodegradation of RhB. In the typical experiment, the sample film to be tested was placed face-up on the holder and 20 ml of RhB solution (the concentration of RhB was 10 mg L^{-1}) was added in the jacketed reactor.

The solution was continuously stirred in the dark for 30 min before light irradiation and the absorbance of the supernatant was measured every 10 minutes until constant indicating the adsorption-desorption equilibrium.

Subsequently, the photocatalytic reaction was performed under a 300 W xenon lamp (PLS-SXE300C). Every 20 min, 3 ml of solution was taken out from the irradiated solution, and then centrifuged at 8000 rpm. Finally, the maximum absorbance at 554 nm of the clarified liquid was measured by UV–Vis spectroscopy (PerkinElmer Lambda 35). At low concentration, the RhB degradation process followed the Langmuir-Hinshelwood kinetic model. The value of the apparent reaction rate constant (k) was calculated from $\ln(C_0/C_t)$ versus irradiation time (t). Here, C_t is the residual concentration of RhB solution and C_0 is the initial concentration.

3 Results and discussion

3.1 Characterization of $\text{Bi}_2\text{MoO}_6/\text{g-CNQDs}$

3.1.1 Structure characteristics

The XRD patterns of Bi_2MoO_6 , g-CNQDs and $\text{Bi}_2\text{MoO}_6/\text{g-CNQDs}$ are shown in Fig. 2. For pure Bi_2MoO_6 , strong characteristic diffraction peaks can be observed at 2θ values of 28.3° , 32.6° , 33.2° , 36.0° , 46.8° , 47.1° , 55.6° , 56.3° and 58.5° , which correspond to the (131), (002), (060), (151), (202), (062), (133), (280) and (262) crystal planes of Bi_2MoO_6 (JCPDS 72-1524), respectively. It is proved that the sample is a pure phase structure, and no other peaks are found. For the g-CNQDs-doped Bi_2MoO_6 sample, the characteristic peak of g-CNQDs ($2\theta = 27.5^\circ$) could not be detected, which may be due to the low content of g-CNQDs in the sample. The XRD patterns of $\text{Bi}_2\text{MoO}_6/\text{g-CNQDs}$

composite catalysts are not significantly different to that of Bi_2MoO_6 , and no other peaks were detected, indicating Bi_2MoO_6 maintains higher crystallinity in composites and the sensitization by g-CNQDs did not change the lattice structure of Bi_2MoO_6 .

Figure 3 shows the SEM images of pure Bi_2MoO_6 as well as $\text{Bi}_2\text{MoO}_6/\text{g-CNQDs}$ composites. The nanosheet structure of Bi_2MoO_6 with homogeneous size is clearly observed in Fig. 3a. After the introduction of g-CNQDs, no significant changes in particle size and morphology of Bi_2MoO_6 were observed (Fig. 3b), confirming that the g-CNQDs material was not incorporated into the lattice of Bi_2MoO_6 . This result is consistent with the XRD pattern.

The microstructure and morphology of the synthesized samples were further investigated by TEM. As shown in Fig. 4, g-CNQDs prepared by acid etching have good dispersion and uniform size, and the particle size was mostly around 3–7 nm. (Fig. 4a). In the TEM image of $\text{Bi}_2\text{MoO}_6/\text{g-CNQDs}$ (Fig. 4b, c), it can be clearly observed that

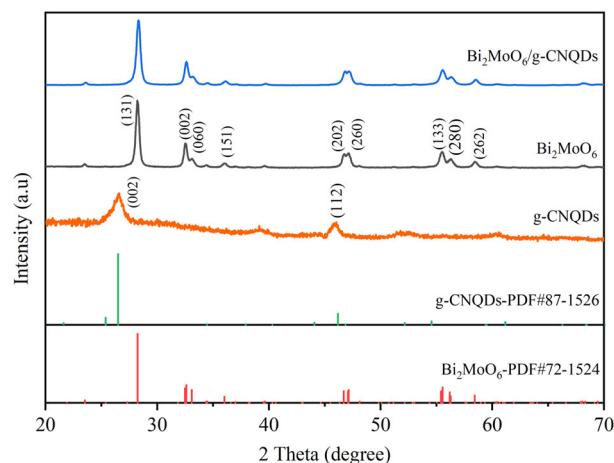


Fig. 2 XRD patterns of g-CNQDs, Bi_2MoO_6 and $\text{Bi}_2\text{MoO}_6/\text{g-CNQDs}$ composite materials

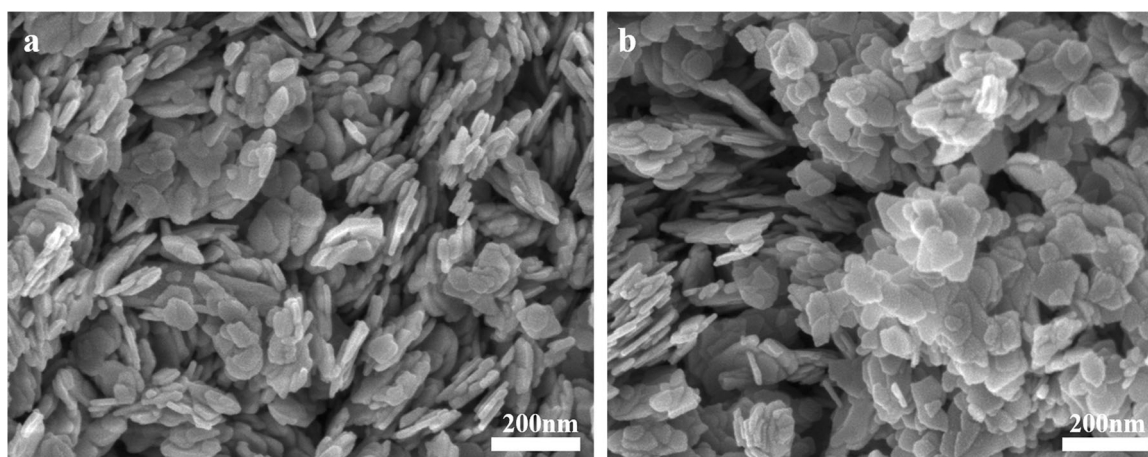


Fig. 3 SEM images of Bi_2MoO_6 **a** and $\text{Bi}_2\text{MoO}_6/\text{g-CNQDs}$ **b**

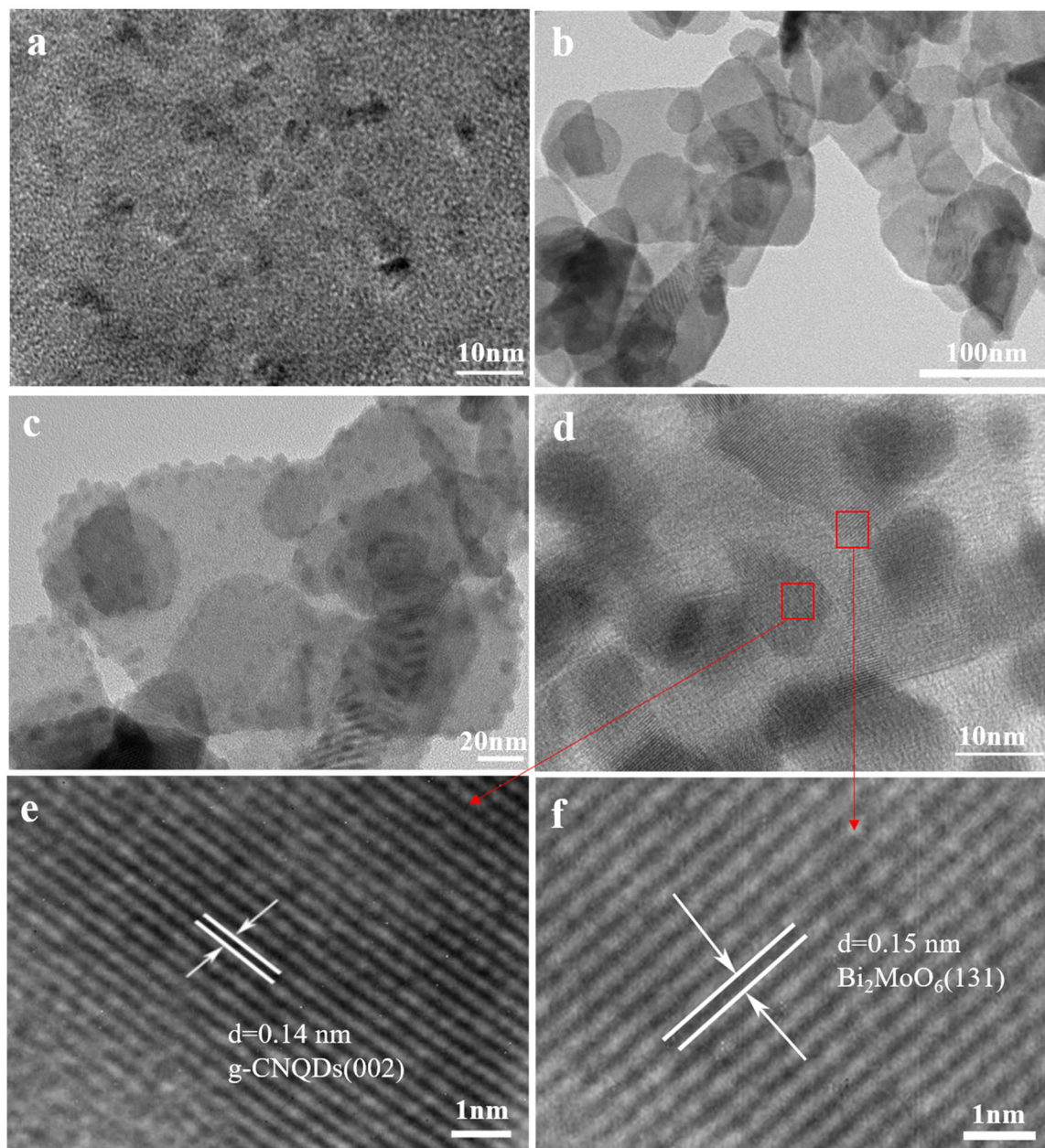


Fig. 4 TEM image of g-CNQDs **a**, $\text{Bi}_2\text{MoO}_6/\text{g-CNQDs}$ **b**, **c**, HRTEM image of $\text{Bi}_2\text{MoO}_6/\text{g-CNQDs}$ **d–f**

g-CNQDs is loaded on the surface of Bi_2MoO_6 . By measuring the lattice fringes of composites in Fig. 4d–f, the crystal plane spacing is about 0.15 nm and 0.14 nm, corresponding to the (131) plane of Bi_2MoO_6 and the (002) plane of g-CNQDs, respectively. Their tight bonding indicates the formation of a heterojunction between g-CNQDs and Bi_2MoO_6 .

The specific surface area and pore volume of as-prepared catalysts were determined by nitrogen adsorption-desorption isotherms measurements. From Fig. 5a, the adsorption isotherms of both pure Bi_2MoO_6 and $\text{Bi}_2\text{MoO}_6/\text{g-CNQDs}$ are type-IV with a distinct hysteresis loop in the

relative pressure range of 0.80–1.00, indicating that the samples are mesoporous materials. The BET specific surface area was calculated as $13.7 \text{ m}^2 \text{ g}^{-1}$ for the pure Bi_2MoO_6 nanosheets and $21.1 \text{ m}^2 \text{ g}^{-1}$ for the $\text{Bi}_2\text{MoO}_6/\text{g-CNQDs}$ composite, showing that the loading of g-CNQDs could increase the specific surface area of Bi_2MoO_6 . It can be observed in Fig. 5b that the pore size distribution was essentially unchanged after the loading of g-CNQDs on Bi_2MoO_6 . Based on the above analysis, the pore structure of Bi_2MoO_6 in the composite photocatalyst was not destroyed and the adsorption performance should be improved by the increase of specific surface area.

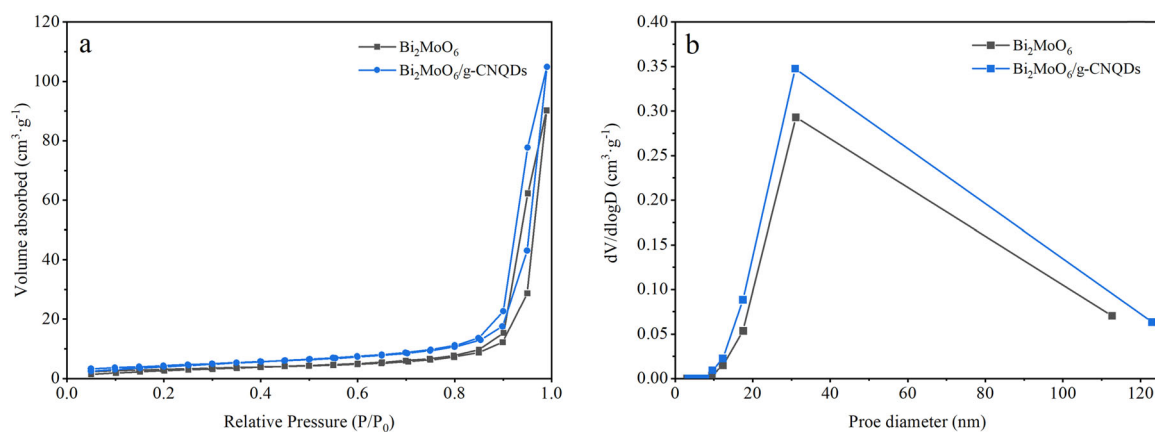


Fig. 5 **a** Nitrogen adsorption/desorption isotherm; **b** pore size distribution of sample

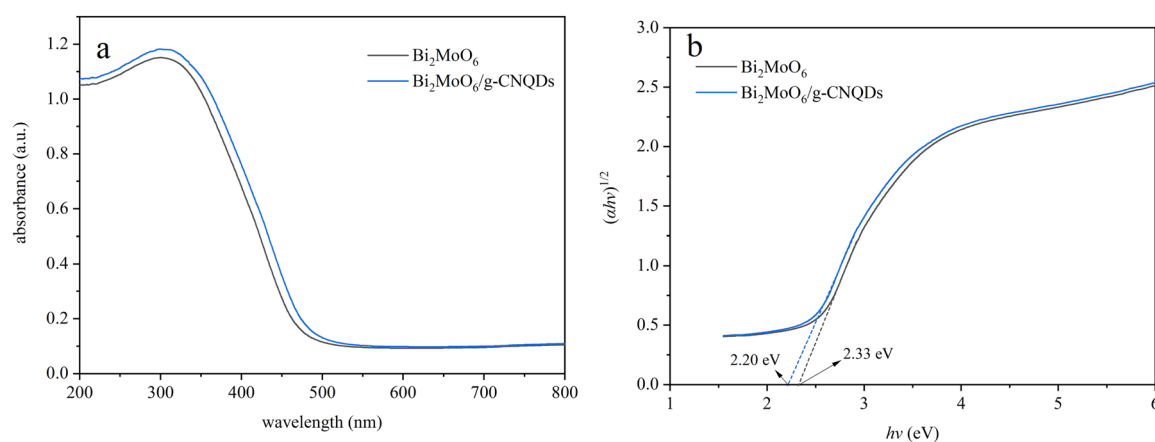


Fig. 6 **a** UV-Vis DRS spectra of samples and **b** the corresponding Tauc's plots

3.1.2 Photoelectric property

The optical absorption of photocatalysts was examined by UV-Vis DRS spectroscopy, and the results were presented in Fig. 6a. It was obvious that Bi₂MoO₆ could absorb visible light below 500 nm to excite electrons. Compared with pure Bi₂MoO₆, the composite Bi₂MoO₆/g-CNQDs has higher visible light absorption intensity, which means that more photons can be absorbed. Besides, the light absorption range of Bi₂MoO₆/g-CNQDs shifts toward higher wavelengths with significantly enhanced intensity when g-CNQDs are introduced. It indicates that more electrons and holes are generated under visible light irradiation. The band gap energy (E_g) of the prepared samples were calculated based on the UV-DRS results, as shown in Fig. 6b. The estimated E_g of Bi₂MoO₆ and Bi₂MoO₆/g-CNQDs are 2.33 eV and 2.20 eV, respectively [52]. Therefore, it can be concluded that the introduction of g-CNQDs can reduce the E_g of the composites and thus improve the absorption of visible light.

In addition, the conduction band edge (E_{CB}) of Bi₂MoO₆ and Bi₂MoO₆/g-CNQDs were estimated by Mott-Schottky

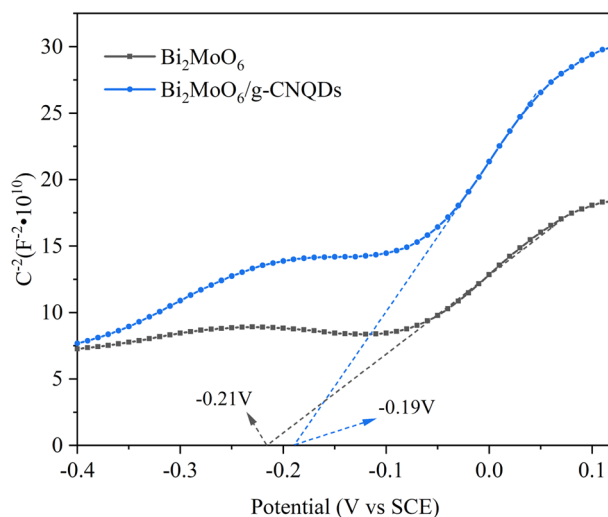


Fig. 7 The Mott-Schottky plots for estimating flat-band potentials of the as-prepared samples

plots (Fig. 7). The positive slope of the curves for both materials proves that the prepared Bi₂MoO₆ and Bi₂MoO₆/

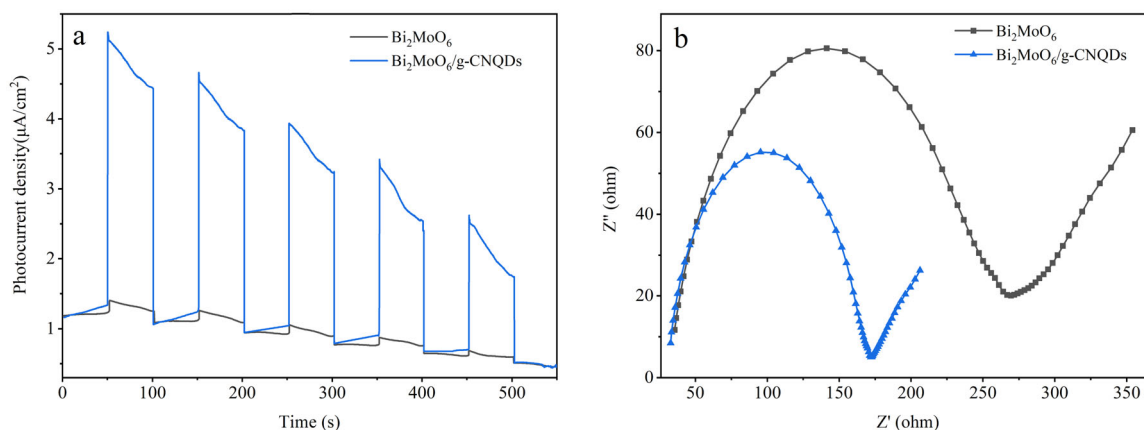


Fig. 8 Transient photocurrent responses **a** and Nyquist plots **b** of Bi₂MoO₆ and Bi₂MoO₆/g-CNQDs

g-CNQDs photocatalysts are n-type semiconductors. Moreover, the flat-band potentials of Bi₂MoO₆ and Bi₂MoO₆/g-CNQDs were estimated to be -0.21 (vs. SCE) and -0.19 V (vs. SCE), respectively. In general, E_{CB} of n-type semiconductors is considered to be more negative than the flat band potentials by approximately 0.2 V [53, 54]. So, based on the above analysis, the E_{CB} of Bi₂MoO₆ and Bi₂MoO₆/g-CNQDs at pH = 7 were calculated to be about -0.41 V (vs. SCE) and -0.39 V (vs. SCE), respectively, which are equal to -0.17 V (vs. normal hydrogen electrode (NHE)) and -0.15 V (vs. NHE), respectively. Furthermore, based on the obtained E_g values, the valence band edges (E_{VB}) of the samples were thus calculated to be 2.16 and 2.05 V.

To study the charge transfer and electrical conductivity of the prepared nanocomposites, transient photocurrent response and electrochemical impedance spectra (EIS) were measured. As shown in Fig. 8a, Bi₂MoO₆/g-CNQDs showed the highest photocurrent density with improved photon response and more electrons generated and transferred compared to pure Bi₂MoO₆. It is again demonstrated that is the introduction of g-CNQDs is very effective to the charge transfer through the successfully constructed heterojunction between Bi₂MoO₆ and g-CNQDs. The Nyquist impedance spectra (Fig. 8b) exhibit that Bi₂MoO₆/g-CNQDs possesses the smallest arc radius, that is better electrical conductivity, indicating that sensitization of g-CNQDs on Bi₂MoO₆ can effectively increase the separation rate and transfer rate of photogenerated electron-hole pairs [55]. The possible inference is that the photogenerated electrons can be easily transferred from the conduction band of g-CNQDs to that of Bi₂MoO₆ because of the more negative conduction band position of g-CNQDs compared to that of Bi₂MoO₆, and thus effectively improve the separation efficiency of the photogenerated electron-hole pairs.

The properties of photogenerated carriers in Bi₂MoO₆/g-CNQDs electrodes was further analyzed by

photoluminescence (PL). Generally, the light-induced recombination of electron-hole pairs leads to PL emission, which means that a stronger fluorescence intensity implies faster recombination of electron-hole pairs [56]. As the absorption edge of Bi₂MnO₆ is 500 nm, light with a wavelength of less than 500 nm should be used as the excitation light in the PL measurement. In the excitation spectra, the strongest fluorescence was emitted at an excitation wavelength of about 420 nm, so the excitation wavelength in emission spectra was set as 420 nm. The measured fluorescence spectrum range in the experiment is from 448 nm to 530 nm. On one hand, the emission wavelength would be longer than the excitation wavelength as result of the Stoke Shift. On the other hand, different fluorescence will be emitted when the excited electrons return from different vibrational energy levels to the ground state. In addition, to eliminate the effect of fluorescence absorbed by sample itself and maintain a consistent measurement baseline, the amount of powder sample in the measurement is kept constant and its absorbance at 448–530 nm is less than 0.3, ensuring that absorbance has little influence on the fluorescence spectrum.

As shown in Fig. 9, it can be seen that the PL intensity of Bi₂MoO₆/g-CNQDs is lower than that of pure Bi₂MoO₆, suggesting a lower electron-hole recombination rate in Bi₂MoO₆/g-CNQDs. This proves that the introduction of g-CNQDs is very effective in inhibiting the recombination of photogenerated electron-hole pairs. Combined with the enhanced absorbance of Bi₂MoO₆/g-CNQDs at 448–530 nm, which also proves that the sensitization of g-CNQDs is successful, it can be inferred that the composite Bi₂MoO₆/g-CNQDs would absorb more sunlight and thus more photogenerated electron-hole pairs would be photogenerated. The combined effect of high generation rate and low recombination rate of photogenerated carriers should bring about significant enhancement in the photocatalytic performance of Bi₂MoO₆/g-CNQDs.

3.2 Characterization of Bi₂MoO₆/g-CNQDs/SiO₂ PCs composite films

3.2.1 SiO₂ microspheres size

In order to investigate the effect of PCs on the photocatalytic activity of Bi₂MoO₆/g-CNQDs, SiO₂ opal PCs with different PBG were prepared. Three case with different relative locations between PBG of PCs and absorption edge of the photocatalyst were investigated: complete overlap, partial overlap and complete non-overlap. To construct the above designed PBG, SiO₂

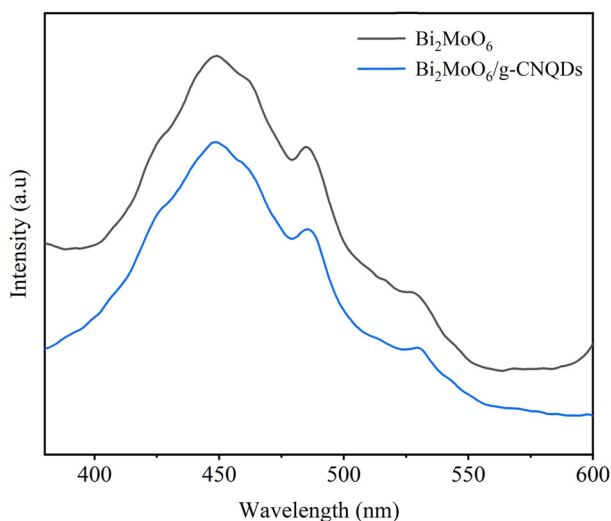


Fig. 9 PL spectra of the as-prepared samples

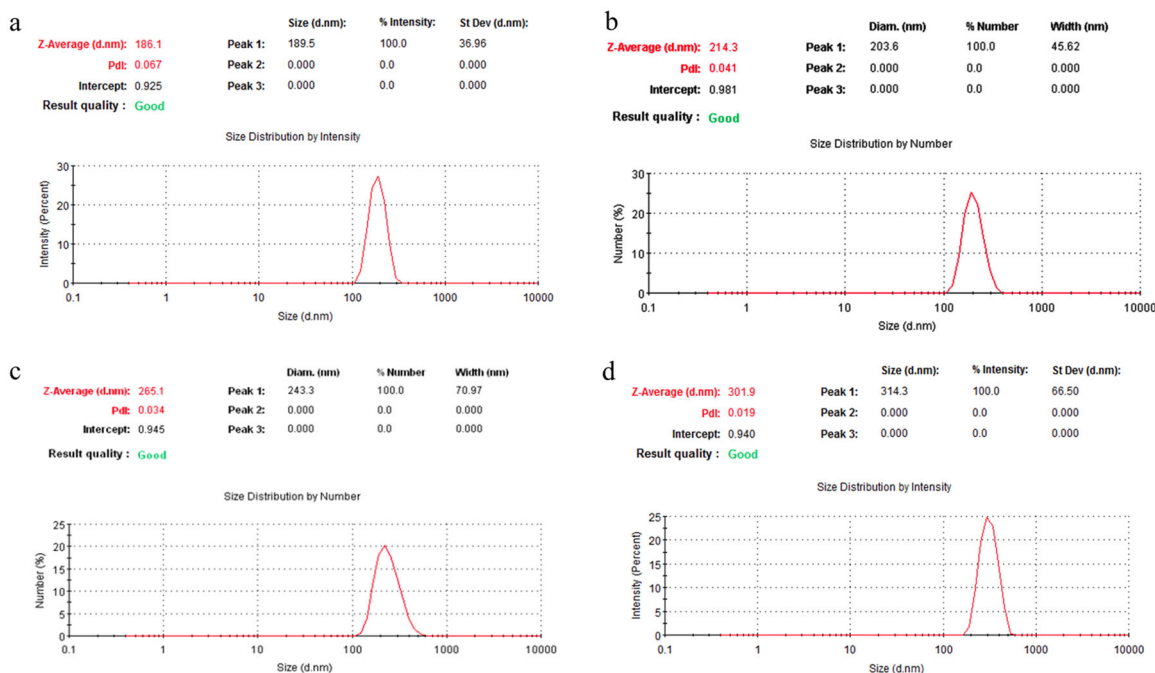


Fig. 10 Dynamic light scattering (DLS) measurements of SiO₂ microspheres with different diameters. **a** 186 nm, **b** 214 nm, **c** 265 nm, and **d** 301 nm

PCs were self-assembled using SiO₂ microspheres with average diameters of 186, 214, 265 and 301 nm, respectively, as shown in Fig. 10(a-d). The polydispersity index, Pdl, is less than 0.06 in all cases, indicating that their monodispersity is very good, and SiO₂ opal PCs with high quality can be obtained by assembling these SiO₂ microspheres.

3.2.2 Optical property

The transmission spectra of all SiO₂ opal PCs are shown in Fig. 11a. It is clear that when the wavelength of light lies in the PBG range, a sharp decrease in the transmittance is evident. That is, the light in the PBG wavelength region is reflected back to and then reabsorbed by the upper layer of photocatalysts, which is beneficial to improving the light utilization. The PBGs of SiO₂ PCs prepared from microspheres with diameters of 186, 214, 265 and 301 nm were observed at the centers of 365, 464, 531 and 612 nm, respectively, named as SiO₂ PCs-365, SiO₂ PCs-464, SiO₂ PCs-531, and SiO₂ PCs-612, respectively. The PBGs of the SiO₂ opal PCs were close to the values calculated from the modified Bragg's law [48]:

$$\lambda = 2\sqrt{\frac{2}{3}}D\sqrt{n_{\text{SiO}_2}^2 f + n_{\text{air}}^2(1-f) - \sin^2\theta}, \quad (1)$$

where λ is the wavelength of the PBG, D is the diameter of the SiO₂ microsphere, n_{SiO_2} (1.45) and n_{air} (1.0) are the refractive index of SiO₂ and air respectively, f is the volume fraction of the SiO₂ phase and its theoretical value is 0.74 for opal materials, and θ is the angle between the incident light vector and the normal of the SiO₂ PCs plane. In the

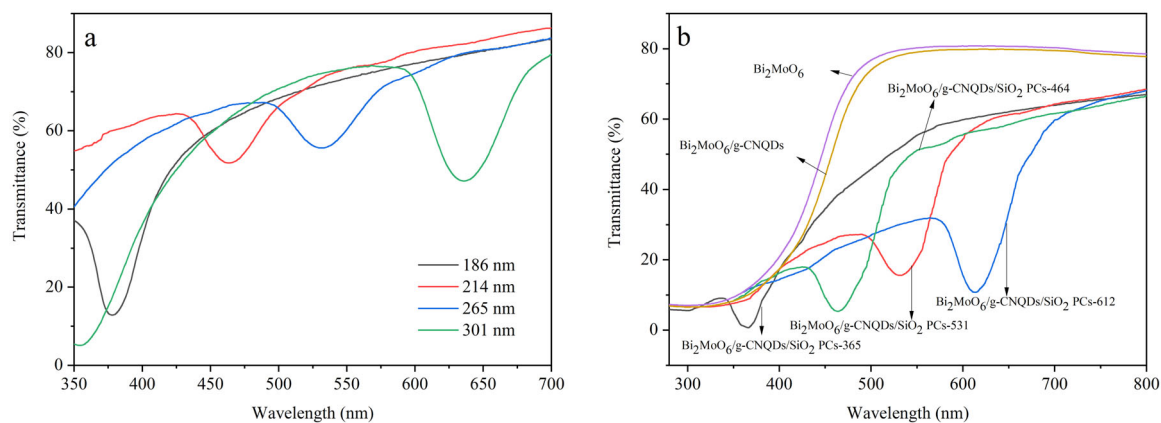


Fig. 11 **a** UV–Vis transmission spectra of SiO₂ PCs assembled using SiO₂ microspheres with different particle sizes (186, 214, 265 and 301 nm); **b** Transmittance of Bi₂MoO₆/g-CNQDs/SiO₂ PCs composite films

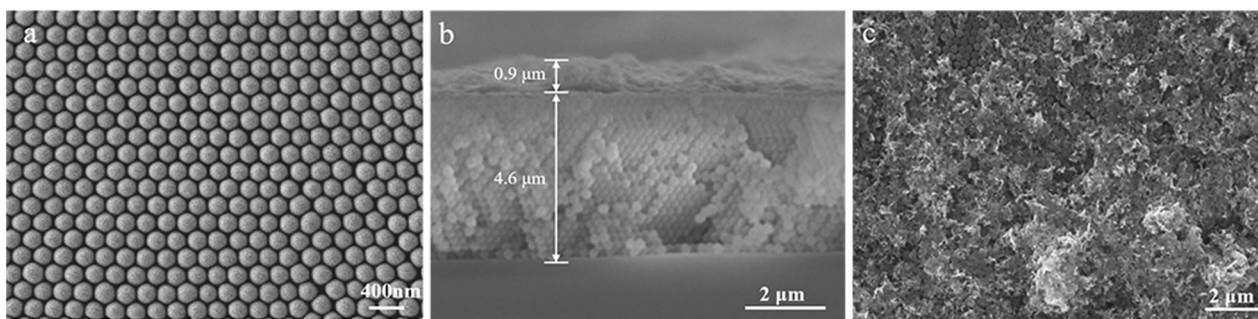


Fig. 12 SEM of SiO₂ PCs self-assembled by 214 nm SiO₂ microspheres **a** and the Bi₂MoO₆/g-CNQDs/SiO₂ PCs-464 composite films: **b** Cross-sectional view; **c** Top view

Table 1 The calculated and measured value of PBGs of SiO₂ Opal

Diameter of SiO ₂ microspheres/nm	PBG of SiO ₂ Opal/nm	
	Calculated	Measured
186	409	365
214	470	464
265	583	531
301	662	612

experiment, the incident light is perpendicular to the photonic crystal plane, where $\theta = 0$.

The PBGs positions of the PCs assembled by SiO₂ microspheres of different particle size were calculated and measured via UV- Vis spectroscopy, as shown in Table 1. The measured PBGs value do not differ much from the calculated one with the refractive index of pure silica, indicating the high quality of the assembled SiO₂ opal PCs and the adjustable PBGs of PCs.

To elucidate the effects of SiO₂ PCs on the light absorption properties of Bi₂MoO₆/g-CNQDs thin films, the transmittance of Bi₂MoO₆/g-CNQDs/SiO₂ PCs composite

films were investigated (Fig. 11b). By further compositing with PCs, the transmittance is significantly reduced in the range of 440–500 nm because the light near the PBG of 464 nm was reflected back and this part of light was reabsorbed by the Bi₂MoO₆/g-CNQDs layer.

3.2.3 Morphology

The morphology and stereo structure of the SiO₂ PCs self-assembled using 214 nm microspheres were observed by SEM, as shown in Fig. 12a. It is observed that the prepared SiO₂ microspheres have a uniform particle size distribution and are tightly bound to each other in a highly ordered face-centered cubic structure. Figure 12c shows the SEM top view of Bi₂MoO₆/g-CNQDs/SiO₂ PCs-464 composite. Comparing with the SiO₂ PCs (Fig. 12a), it can be seen that Bi₂MoO₆/g-CNQDs is uniformly distributed and form a dense and flat layer on the surface of the SiO₂ PCs. Meanwhile, the cross-section of the composite film in Fig. 12b shows that the upper layer of Bi₂MoO₆/g-CNQDs is flat and the thickness is about 0.9 μm, the lower layer is densely filled with about 20 layers of SiO₂ microspheres with a

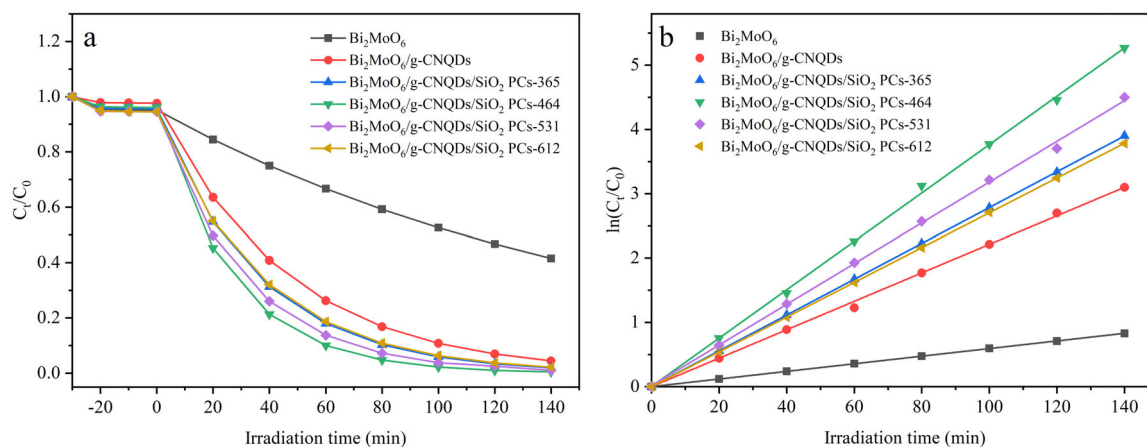


Fig. 13 Photocatalytic degradation of RhB on Bi_2MoO_6 , $\text{Bi}_2\text{MoO}_6/\text{g-CNQDs}$ and $\text{Bi}_2\text{MoO}_6/\text{g-CNQDs}/\text{SiO}_2$ PCs composite films **a** Curves of degradation efficiency; **b** First order dynamics simulation curves

Table 2 Kinetic constants of photocatalytic degradation of RhB on different samples

Catalyst	Kinetic constants (min^{-1})	Linear dependence (R^2)	Enhancement
Bi_2MoO_6	0.00628	0.99854	1
$\text{Bi}_2\text{MoO}_6/\text{g-CNQDs}$	0.02241	0.9998	3.56
$\text{Bi}_2\text{MoO}_6/\text{g-CNQDs}/\text{SiO}_2$ PCs -365	0.02725	0.99985	4.34
$\text{Bi}_2\text{MoO}_6/\text{g-CNQDs}/\text{SiO}_2$ PCs -464	0.03634	0.99875	5.59
$\text{Bi}_2\text{MoO}_6/\text{g-CNQDs}/\text{SiO}_2$ PCs -531	0.03181	0.99903	5.07
$\text{Bi}_2\text{MoO}_6/\text{g-CNQDs}/\text{SiO}_2$ PCs -612	0.02596	0.99875	4.13

Bold entries highlight the sample with the best photocatalytic effect of the above film

thickness of about 4.6 μm . It can also be seen that $\text{Bi}_2\text{MoO}_6/\text{g-CNQDs}$ spin-coated on the surface of SiO_2 PCs does not penetrate into the interstices of SiO_2 PCs and has no effect on the structure and integrity of the PCs.

3.3 Photocatalytic performance

Based on the above analysis, the ternary $\text{Bi}_2\text{MoO}_6/\text{g-CNQDs}/\text{SiO}_2$ PCs photocatalyst can improve the separation and transfer of photogenerated carriers, inhibit the recombination of photogenerated electron–hole pairs and increase light absorbance, which can effectively improve the photocatalytic activity. Figure 13a presents the photocatalytic performance of the $\text{Bi}_2\text{MoO}_6/\text{g-CNQDs}/\text{SiO}_2$ PCs composite films. Firstly, the photocatalytic activity of g-CNQDs sensitized Bi_2MoO_6 nanosheets was significantly enhanced. Then the photocatalytic activity of $\text{Bi}_2\text{MoO}_6/\text{g-CNQDs}$ composited with PCs having different PBGs were further investigated.

Combined with the transmittance spectra of $\text{Bi}_2\text{MoO}_6/\text{g-CNQDs}$ composite catalysts in Fig. 11b, it can be seen that g-CNQDs significantly improve the light harvesting ability of Bi_2MoO_6 for light in the range of 340–500 nm. SiO_2 PCs-464 reflects the light near 464 nm back to $\text{Bi}_2\text{MoO}_6/\text{g-CNQDs}$, and this reflected light can be effectively absorbed

by $\text{Bi}_2\text{MoO}_6/\text{g-CNQDs}$, increasing the photocatalytic degradation rate up to 99%. While SiO_2 PCs-531 can reflect the light located near 531 nm, some of this light is partially absorbed by $\text{Bi}_2\text{MoO}_6/\text{g-CNQDs}$, and the increase of photocatalytic activity is also relatively obvious. In addition, SiO_2 PCs-365 and SiO_2 PCs -612 also have a relatively smaller effect on enhancing the photocatalytic activity. For SiO_2 PCs -365, $\text{Bi}_2\text{MoO}_6/\text{g-CNQDs}$ itself can absorb most of the light at 365 nm, so the reflected light near 365 nm is very limited. For SiO_2 PCs-612, the reflected light at 612 nm is not in the light response range of $\text{Bi}_2\text{MoO}_6/\text{g-CNQDs}$ (<500 nm). Therefore, the photocatalytic degradation rate of the photocatalysts follows the order: $\text{Bi}_2\text{MoO}_6/\text{g-CNQDs}/\text{SiO}_2$ PCs-464 > $\text{Bi}_2\text{MoO}_6/\text{g-CNQDs}/\text{SiO}_2$ PCs-531 > $\text{Bi}_2\text{MoO}_6/\text{g-CNQDs}/\text{SiO}_2$ PCs-365 > $\text{Bi}_2\text{MoO}_6/\text{g-CNQDs}/\text{SiO}_2$ PCs-612 > $\text{Bi}_2\text{MoO}_6/\text{g-CNQDs}$ > Bi_2MoO_6 .

Figure 13b exhibits the dynamic curves of RhB degradation for the prepared composites, and the corresponding kinetic constants of each sample are listed in Table 2. The photocatalytic activity of $\text{Bi}_2\text{MoO}_6/\text{g-CNQDs}$ is 3.56 times higher than that of pure Bi_2MoO_6 . After coupled with SiO_2 PCs, the kinetic constants further increase and that of $\text{Bi}_2\text{MoO}_6/\text{g-CNQDs}/\text{SiO}_2$ PCs-464 were the largest as the bold font in Table 2, 5.59 times higher than that of pure Bi_2MoO_6 . It indicates that g-CNQDs and PCs can

synergistically enhance the photocatalytic activity of Bi_2MoO_6 , and the great enhancement can get when the PBG of PCs is at right location.

The effect of initial pH on the photocatalytic degradation of RhB is investigated in Fig. 14. As the pH of the RhB solution increased, there was a significant decrease in the degradation efficiency. The maximum of RhB adsorption in the dark by the catalyst was also found when the pH was 3.0. When the pH is less than 4.0, RhB in solution is present in the form of cations and monomers [57], which can easily enter the pores of the composite. In contrast for pH greater than 4.0, RhB in solution exists as a zwitterion. It is easy to generate RhB dimers due to the electrostatic attraction between the carboxyl group and xanthene group on the RhB molecule. Consequently, the molecule turns larger and is unable to enter the pores of catalysts, thus reducing the adsorption capacity of the catalyst for RhB. In addition,

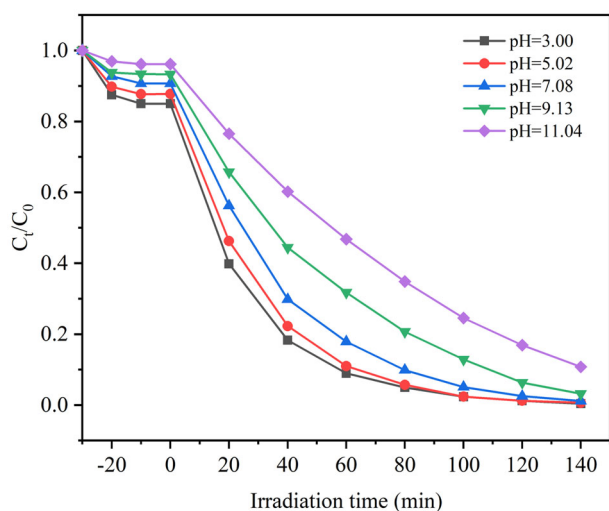


Fig. 14 Effect of initial pH of RhB solution on adsorption and photocatalytic performance of $\text{Bi}_2\text{MoO}_6/\text{g-CNQDs}/\text{SiO}_2$ PCs-464

with the increase of pH, the aromatic carboxylic acid group on RhB will dissociate and the nitrogen-containing group will deprotonate, which will cause electrostatic repulsion between RhB and the catalyst, resulting in a further decrease of adsorption capacity [58].

For the photocatalytic efficiency, it can be seen that the photodegradation rate under acidic conditions is the fastest after reaching the adsorption-desorption equilibrium. The photodegradation efficiency was: $\text{pH} = 3.00 > \text{pH} = 5.02 > \text{pH} = 7.08 > \text{pH} = 9.13 > \text{pH} = 11.04$. This can be attributed to the mutual repulsion between the negatively charged photocatalyst and the electronegative RhB molecule under alkaline conditions, which inhibits the photocatalytic reaction [59]. Consequently, acidic conditions are more favorable for the photocatalytic degradation of RhB on $\text{Bi}_2\text{MoO}_6/\text{g-CNQDs}/\text{SiO}_2$ PCs-464.

Moreover, photocatalysts need not only excellent photocatalytic performance but also sufficient stability, which plays a crucial role in their practical applications. The cycle reproducibility of $\text{Bi}_2\text{MoO}_6/\text{g-CNQDs}/\text{SiO}_2$ PCs-464 degradation of RhB is also investigated in Fig. 15a. The photodegradation efficiency of $\text{Bi}_2\text{MoO}_6/\text{g-CNQDs}/\text{SiO}_2$ PCs-464 composite film after four cycles slightly decreased, indicating that the sample has good photostability under simulated sunlight irradiation. This may be due to the decrease in carbon content in the g-CNQDs, which is oxidized to carbon dioxide after several light cycles. The decrease of carbon content in the photocatalyst makes the sensitization of g-CNQDs less effective, and therefore the photocatalytic effect decreases after four cycles [60, 61]. Meanwhile, as shown in Fig. 15b, by observing the XRD patterns of the $\text{Bi}_2\text{MoO}_6/\text{g-CNQDs}$ composite after four cycles, it can be seen that the diffraction peaks of $\text{Bi}_2\text{MoO}_6/\text{g-CNQDs}$ did not change significantly before and after the cycles, indicating that the crystal structure remained basically unchanged during the photocatalytic reaction.

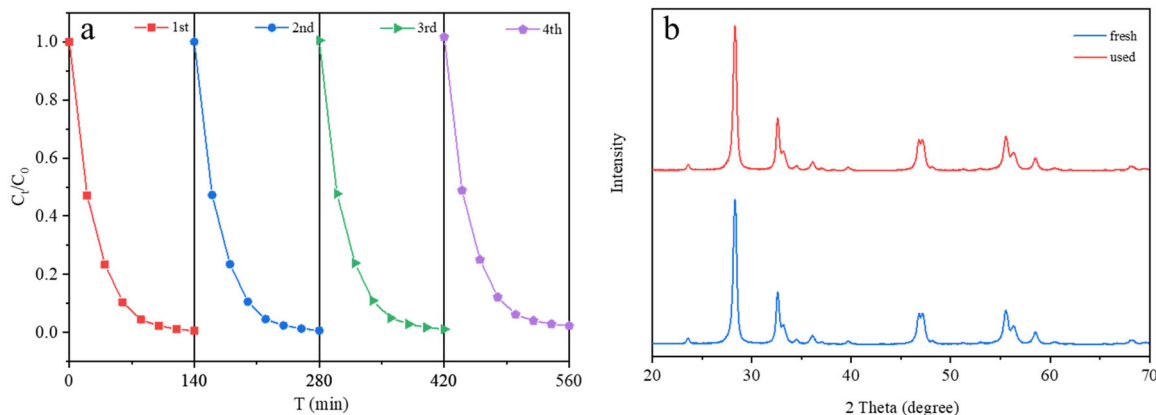


Fig. 15 **a** Test of catalytic cycle stability of $\text{Bi}_2\text{MoO}_6/\text{g-CNQDs}/\text{SiO}_2$ PCs-464 composite film; **b** XRD diagram of $\text{Bi}_2\text{MoO}_6/\text{g-CNQDs}$ composite before and after cycling

Therefore, the as-prepared $\text{Bi}_2\text{MoO}_6/\text{g-CNQDs}/\text{SiO}_2$ PCs-464 composite film photocatalyst has excellent reproducibility and stability.

3.4 Mechanism of the photocatalytic activity enhancement

3.4.1 Active reactive species in photocatalysis

To further investigate the photodegradation mechanism, radical capture experiments were performed to investigate the reactive groups of $\text{Bi}_2\text{MoO}_6/\text{g-CNQDs}$ that play a major role in the photocatalytic degradation of RhB. During the photocatalytic activity test, 0.1 mmol/L of *p*-benzoquinone (BQ), EDTA-2Na and tert-butanol (TBA) were added as trapping agents for superoxide radicals ($\cdot\text{O}_2^-$), photogenerated holes (h^+) and hydroxyl radicals ($\cdot\text{OH}$), respectively. As shown in Fig. 16, the photocatalytic degradation rates of RhB were all reduced after the addition of the trapping agents. The inhibition effect of the three trapping agents is shown as: EDTA-2Na > BQ > TBA. The addition of TBA had a very slight inhibition effect, indicating the role of $\cdot\text{OH}$ in photodegradation is negligible. EDTA-2Na had the most obvious inhibition effect, followed by BQ, indicating $\cdot\text{O}_2^-$ and h^+ had a contribution in the photocatalytic degradation of RhB, while h^+ is the most dominant reactive radical.

3.4.2 Possible synergetic photocatalytic mechanism

For the present enhancement analysis, we propose a mechanism that may be applicable to the photocatalytic degradation of RhB by ternary-structured $\text{Bi}_2\text{MoO}_6/\text{g-CNQDs}/\text{SiO}_2$ PCs, as shown in Fig. 17.

During the photocatalytic process, on one hand, Bi_2MoO_6 can be directly excited by light to produce photogenerated electron-hole pairs. Photogenerated holes on the valence band (VB) of Bi_2MoO_6 can directly degrade RhB. The E_{VB} and E_{CB} of as-synthesized Bi_2MoO_6 are calculated to be 2.16 eV versus NHE and -0.17 eV versus NHE, respectively. The electrons were transferred to generate $\cdot\text{O}_2^-$ due to the more negative CB potential value of Bi_2MoO_6 than the redox potential of $\text{O}_2/\cdot\text{O}_2^-$ (-0.046 V) [62]. In the presence of g-CNQDs, electrons in the CB of photogenerated Bi_2MoO_6 can be transferred to g-CNQDs due to their excellent electron conductivity, which then further reduces O_2 to $\cdot\text{O}_2^-$, with the latter being a powerful oxidative species for RhB degradation. On the other hand, when coupled with PCs and the PBG of SiO_2 PCs matches the absorption band of $\text{Bi}_2\text{MoO}_6/\text{g-CNQDs}$, the SiO_2 PCs can act as Bragg mirrors to reflect the unabsorbed light back to the catalysts to perform secondary light absorption, thus

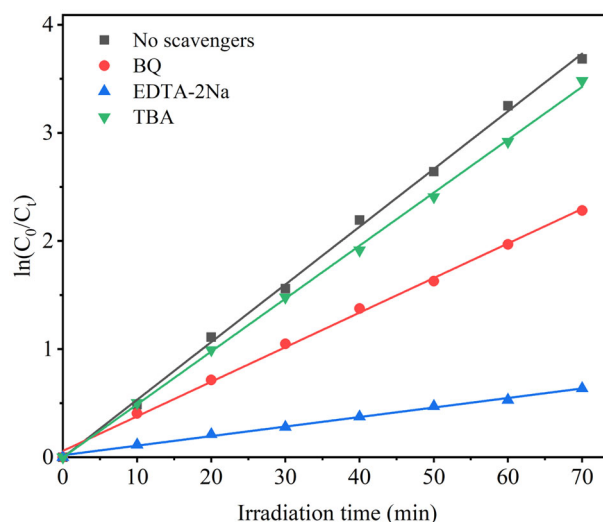


Fig. 16 The trapping experiments in RhB photodegradation over $\text{Bi}_2\text{MoO}_6/\text{g-CNQDs}$

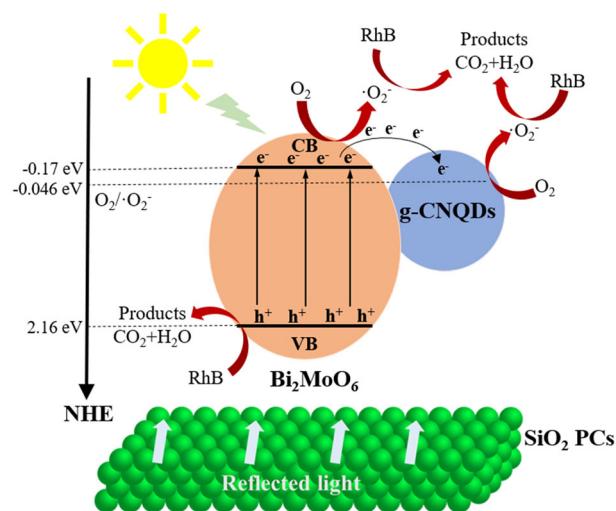


Fig. 17 The proposed schematic diagram for the photocatalytic degradation of RhB by $\text{Bi}_2\text{MoO}_6/\text{g-CNQDs}/\text{SiO}_2$ PCs composites under simulated sunlight irradiation

enhancing light harvesting. In the end, the synergistic effect of g-CNQDs and SiO_2 PCs can effectively improve the photocatalytic performance of Bi_2MoO_6 .

4 Conclusions

Ternary composite photocatalysts of $\text{Bi}_2\text{MoO}_6/\text{g-CNQDs}/\text{SiO}_2$ -PCs with promising applications for enhanced light harvesting were successfully prepared. The sensitization with g-CNQDs enhances the photocatalytic activity of Bi_2MoO_6 by a factor of 3.56. The sensitization of g-CNQDs broadens the light response up to 500 nm. At the same time, the

construction of heterojunctions between Bi_2MoO_6 and g-CNQDs improves the separation efficiency of photo-generated electron-hole pairs and retain h^+ and e^- with sufficient potential to participate in the degradation of organic species.

After compositing with SiO_2 PCs, the photocatalytic activity was further enhanced. The PBG reflection effect and scattering effect contributes to the enhancement. The enhancement of photocatalytic activity was highest and 5.59 times that of pure Bi_2MoO_6 when the PBG of PCs was matched to the absorption range of the $\text{Bi}_2\text{MoO}_6/\text{g-CNQDs}$ at 464 nm. This work provides a simple and effective method for the synthesis of thin-film photocatalysts and demonstrates that matching of the electronic band gap of the semiconductor with PBG of the PCs is the key to improve photocatalytic performance.

Acknowledgements This research work was supported by the National Natural Science Foundation of China (51502210), the Fund of Key Laboratory of Catalysis and Energy Materials Chemistry of Ministry of Education & Hubei Key Laboratory of Catalysis and Materials Science (CHCL21002), the Innovation Project of Engineering Research Center of Phosphorus Resources Development and Utilization of Ministry of Education (LCX2021001), the Innovation Project of Hubei Three Gorges Laboratory (SC211003) and the 16th President's Foundation of Wuhan Institute of Technology (XZJJ2021091), the 2021 Hubei College Students Innovation and Entrepreneurship Training Program (S202110490001).

Compliance with ethical standards

Conflict of interest The authors declare no competing interests.

References

- Patel M, Kumar R, Kishor K, Mlsna T, Pittman CU, Mohan D (2019) Pharmaceuticals of emerging concern in aquatic systems: chemistry, occurrence, effects, and removal methods. *Chem Rev* 119:3510–3673. <https://doi.org/10.1021/acs.chemrev.8b00299>
- Srikanth B, Goutham R, Narayan RB, Ramprasad A, Gopinath KP, Sankaranarayanan AR (2017) Recent advancements in supporting materials for immobilised photocatalytic applications in waste water treatment. *J Environ Manag* 200:60–78. <https://doi.org/10.1016/j.jenvman.2017.05.063>
- Marinho BA, de Souza SMAGU, de Souza AAU, Hotza D (2021) Electrospun TiO_2 nanofibers for water and wastewater treatment: a review. *J Mater Sci* 56:5428–5448. <https://doi.org/10.1007/s10853-020-05610-6>
- Ebrahimi M, Akhavan O (2022) Nanomaterials for photocatalytic degradations of analgesic, mucolytic and anti-biotic/viral/inflammatory drugs widely used in controlling SARS-CoV-2. *Catalysts* 12:667. <https://doi.org/10.3390/catal12060667>
- Yang JH, Wang DG, Han HX, Li C (2013) Roles of cocatalysts in photocatalysis and photoelectrocatalysis. *Acc Chem Res* 46:1900–1909. <https://doi.org/10.1021/ar300227e>
- Rafiq A, Ikram M, Ali S, Niaz F, Khan M, Khan Q, Maqbool M (2021) Photocatalytic degradation of dyes using semiconductor photocatalysts to clean industrial water pollution. *J Ind Eng Chem* 97:111–128. <https://doi.org/10.1016/j.jiec.2021.02.017>
- Som I, Roy M, Saha R (2020) Advances in nanomaterial-based water treatment approaches for photocatalytic degradation of water pollutants. *ChemCatChem* 12:3409–3433. <https://doi.org/10.1002/cctc.201902081>
- Basavarajappa PS, Patil SB, Ganganagappa N, Reddy KR, Raghu AV, Reddy CV (2020) Recent progress in metal-doped TiO_2 , non-metal doped/codoped TiO_2 and TiO_2 nanostructured hybrids for enhanced photocatalysis. *Int J Hydrog Energy* 45:7764–7778. <https://doi.org/10.1016/j.ijhydene.2019.07.241>
- Mendoza-Mendoza E, Nunez-Briones AG, Garcia-Cerda LA, Peralta-Rodriguez RD, Montes-Luna AJ (2018) One-step synthesis of ZnO and Ag/ZnO heterostructures and their photocatalytic activity. *Ceram Int* 44:6176–6180. <https://doi.org/10.1016/j.ceramint.2018.01.001>
- Yang MJ, Li J, Ke GL, Liu BY, Dong FQ, Yang L, He HC, Zhou Y (2021) WO_3 homojunction photoanode: Integrating the advantages of WO_3 different facets for efficient water oxidation. *J Energy Chem* 56:37–45. <https://doi.org/10.1016/j.jechem.2020.07.059>
- Humayun M, Raziq F, Khan A, Luo W (2018) Modification strategies of TiO_2 for potential applications in photocatalysis: a critical review. *Green Chem Lett Rev* 11:86–102. <https://doi.org/10.1080/17518253.2018.1440324>
- Zahid AH, Han QF (2021) A review on the preparation, microstructure, and photocatalytic performance of Bi_2O_3 in polymorphs. *Nanoscale* 13:17687–17724. <https://doi.org/10.1039/d1nr03187b>
- Shokraiyani J, Jahed V, Rabbani M (2021) Study of photocatalytic activity of Bi_2WO_6 tire-like microstructure. *J Chin Chem Soc* 68:1880–1886. <https://doi.org/10.1002/jccs.202100176>
- Bijanazad K, Tadjarodi A, Akhavan O, Khiavi MM (2016) Solid state preparation and photocatalytic activity of bismuth oxybromide nanoplates. *Res Chem Intermed* 42:2429–2447. <https://doi.org/10.1007/s11164-015-2159-2>
- Jia YL, Lin YH, Ma Y, Shi WB (2019) Fabrication of hollow Bi_2MoO_6 nanorods with efficient photocatalytic performance. *Mater Lett* 234:83–86. <https://doi.org/10.1016/j.matlet.2018.09.081>
- Wu XL, Ng YH, Wen XM, Chung HY, Wong RJ, Du Y, Dou SX, Amal R et al. (2018) Construction of a $\text{Bi}_2\text{MoO}_6/\text{Bi}_2\text{Mo}_3\text{O}_{12}$ heterojunction for efficient photocatalytic oxygen evolution. *Chem Eng J* 353:636–644. <https://doi.org/10.1016/j.cej.2018.07.149>
- Wang J, Sun YG, Wu CC, Cui Z, Rao PH (2019) Enhancing photocatalytic activity of Bi_2MoO_6 via surface co-doping with Ni^{2+} and Ti^{4+} ions. *J Phys Chem Solids* 129:209–216. <https://doi.org/10.1016/j.jpcs.2019.01.014>
- Shimodaira Y, Kato H, Kobayashi H, Kudo A (2006) Photo-physical properties and photocatalytic activities of bismuth molybdates under visible light irradiation. *J Phys Chem B* 110:17790–17797. <https://doi.org/10.1021/jp0622482>
- Zhou L, Wang WZ, Zhang LS (2007) Ultrasonic-assisted synthesis of visible-light-induced Bi_2MO_6 ($\text{M} = \text{W}, \text{Mo}$) photocatalysts. *J Mol Catal A Chem* 268:195–200. <https://doi.org/10.1016/j.molcata.2006.12.026>
- Peng YH, Zhang Y, Tian FH, Zhang JQ, Yu JQ (2017) Structure tuning of Bi_2MoO_6 and their enhanced visible light photocatalytic performances. *Crit Rev Solid State Mater Sci* 42:347–372. <https://doi.org/10.1080/10408436.2016.1200009>
- Yin GL, Jia YL, Lin YH, Zhang CY, Zhu ZH, Ma Y (2022) A review on hierarchical Bi_2MoO_6 nanostructures for photocatalysis applications. *N J Chem* 46:906–918. <https://doi.org/10.1039/d1nj04705a>
- Xing YX, Gao XC, Ji GF, Liu ZL, Du CF (2018) Synthesis of carbon doped Bi_2MoO_6 for enhanced photocatalytic performance and tumor photodynamic therapy efficiency. *Appl Surf Sci* 465:369–382. <https://doi.org/10.1016/j.apsusc.2018.09.200>
- Di J, Xia JX, Ji MX, Li HP, Xu H, Li HM, Chen R (2015) The synergistic role of carbon quantum dots for the improved

- photocatalytic performance of Bi_2MoO_6 . *Nanoscale* 7:11433–11443. <https://doi.org/10.1039/C5NR01350J>
24. Kandi D, Marthar A, Thirumurugan A, Parida KM (2017) CdS QDs-decorated self-doped $\gamma\text{-Bi}_2\text{MoO}_6$: a sustainable and versatile photocatalyst toward photoreduction of Cr (VI) and degradation of phenol. *ACS Omega* 2:9040–9056. <https://doi.org/10.1021/acsomega.7b01250>
 25. Li H, Zhang TX, Pan C, Pu CC, Hu Y, Hu XY, Liu EZ, Fan J (2017) Self-assembled $\text{Bi}_2\text{MoO}_6/\text{TiO}_2$ nanofiber heterojunction film with enhanced photocatalytic activities. *Appl Surf Sci* 391:303–310. <https://doi.org/10.1016/j.apsusc.2016.06.167>
 26. Han G, Li DY, Zheng YF, Song XC (2018) Enhanced visible-light-responsive photocatalytic properties of $\text{Bi}_2\text{MoO}_6\text{-BiOCl}$ nanoplate composites. *J Nanosci Nanotechnol* 18:5575–5581. <https://doi.org/10.1166/jnn.2018.15379>
 27. Hu TP, Yang Y, Dai K, Zhang JF, Liang CH (2018) A novel Z-scheme $\text{Bi}_2\text{MoO}_6/\text{BiOBr}$ photocatalyst for enhanced photocatalytic activity under visible light irradiation. *Appl Surf Sci* 456:473–481. <https://doi.org/10.1016/j.apsusc.2018.06.186>
 28. Xiao K, Huang HW, Tian N, Zhang YH (2016) Mixed-calcination synthesis of $\text{Bi}_2\text{MoO}_6/\text{g-C}_3\text{N}_4$ heterojunction with enhanced visible-light-responsive photoreactivity for RhB degradation and photocurrent generation. *Mater Res Bull* 83:172–178. <https://doi.org/10.1016/j.materresbull.2016.05.016>
 29. Tian YL, Cheng FX, Zhang X, Yan F, Zhou BC, Chen Z, Liu JY, Xi FN et al. (2014) Solvothermal synthesis and enhanced visible light photocatalytic activity of novel graphitic carbon nitride– Bi_2MoO_6 heterojunctions. *Powder Technol* 267:126–133. <https://doi.org/10.1016/j.powtec.2014.07.021>
 30. Kim JH, Ma A, Jung H, Kim HY, Choe HR, Kim YH, Nam KM (2019) In situ growth of the Bi_2S_3 nanowire array on the Bi_2MoO_6 film for an improved photoelectrochemical performance. *ACS Omega* 4:17359–17365. <https://doi.org/10.1021/acsomega.9b02111>
 31. He L, Lv H, Ma LF, Li WN, Si JQ, Ikram M, Ullah M, Wu HY et al. (2020) Controllable synthesis of intercalated $\gamma\text{-Bi}_2\text{MoO}_6/\text{graphene}$ nanosheet composites for high performance NO_2 gas sensor at room temperature. *Carbon* 157:22–32. <https://doi.org/10.1016/j.carbon.2019.10.011>
 32. Yang Q, Guo EY, Liu H, Lu QF (2019) Engineering of Z-scheme 2D/3D architectures with Bi_2MoO_6 on TiO_2 nanosphere for enhanced photocatalytic 4-nitrophenol degradation. *J Taiwan Inst Chem E* 105:65–74. <https://doi.org/10.1016/j.jtice.2019.09.024>
 33. Abdellatif HRS, Zhang G, Wang XT, Xie DT, Irvine JTS, Ni JP, Ni CS (2019) Boosting photocatalytic oxidation on graphitic carbon nitride for efficient photocatalysis by heterojunction with graphitic carbon units. *Chem Eng J* 370:875–884. <https://doi.org/10.1016/j.cej.2019.03.266>
 34. Qi KZ, Liu SY, Zada A (2020) Graphitic carbon nitride, a polymer photocatalyst. *J Taiwan Inst Chem E* 109:111–123. <https://doi.org/10.1016/j.jtice.2020.02.012>
 35. Tang YR, Su YY, Yang N, Zhang LC, Lv Y (2014) Carbon nitride quantum dots: a novel chemiluminescence system for selective detection of free chlorine in water *Anal Chem* 86(9):4528–4535. <https://doi.org/10.1021/ac5005162>
 36. Sun TT, Yu XM, Zhong SW, Xu L, Zhao YH (2020) Late-model g-CNQDs/ $\text{H}_3\text{PW}_{12}\text{O}_{40}/\text{TiO}_2$ heterojunction nanocatalyst with enhanced photocatalytic performance. *J Mater Sci* 55:15152–15166. <https://doi.org/10.1007/s10853-020-05083-7>
 37. Chan MH, Chen CW, Lee IJ, Chan YC, Tu DT, Hsiao M, Chen CH, Chen XY et al. (2016) Near-infrared light-mediated photodynamic therapy nanoplatfrom by the electrostatic assembly of upconversion nanoparticles with graphitic carbon nitride quantum dots. *Inorg Chem* 55:10267–10277. <https://doi.org/10.1021/acs.inorgchem.6b01522>
 38. Li YH, Lv KL, Ho WK, Dong F, Wu XF, Xia Y (2017) Hybridization of rutile TiO_2 (rTiO_2) with g- C_3N_4 quantum dots (CN QDs): an efficient visible-light-driven Z-scheme hybridized photocatalyst. *Appl Catal B Environ* 202:611–619. <https://doi.org/10.1016/j.apcatb.2016.09.055>
 39. Chen SB, Hao N, Jiang D, Zhang X, Zhou Z, Zhang Y, Wang K (2017) Graphitic carbon nitride quantum dots in situ coupling to Bi_2MoO_6 nanohybrids with enhanced charge transfer performance and photoelectrochemical detection of copper ion. *J Electroanal Chem* 787:66–71. <https://doi.org/10.1016/j.jelechem.2017.01.042>
 40. Collins G, Armstrong E, McNulty D, O'Hanlon S, Geaney H, O'Dwyer C (2016) 2D and 3D photonic crystal materials for photocatalysis and electrochemical energy storage and conversion. *Sci Technol Adv Mater* 17:563–582. <https://doi.org/10.1080/14686996.2016.1226121>
 41. Deparis O, Mouchet SR, Su BL (2015) Light harvesting in photonic crystals revisited: why do slow photons at the blue edge enhance absorption. *Phys Chem Chem Phys* 17:30525–30532. <https://doi.org/10.1039/c5cp04983k>
 42. Wu M, Jin J, Liu J, Deng Z, Li Y, Deparis O, Su BL (2013) High photocatalytic activity enhancement of titania inverse opal films by slow photon effect induced strong light absorption. *J Mater Chem A* 1:15491–15500. <https://doi.org/10.1039/c3ta13574h>
 43. Liu J, Jin J, Li Y, Huang HW, Wang C, Wu M, Chen LH, Su BL (2014) Tracing the slow photon effect in a ZnO inverse opal film for photocatalytic activity enhancement. *J Mater Chem A* 2:5051–5059. <https://doi.org/10.1039/c3ta15044e>
 44. Wu XJ, Lan DP, Zhang RF, Pang F, Ge JP (2019) Fabrication of opaline ZnO photonic crystal film and its slow-photon effect on photoreduction of carbon dioxide. *Langmuir* 35:194–202. <https://doi.org/10.1021/acs.langmuir.8b03327>
 45. Rahul TK, Sandhyarani N (2015) Nitrogen-fluorine co-doped titania inverse opals for enhanced solar light driven photocatalysis. *Nanoscale* 7:19743. <https://doi.org/10.1039/c5nr04663g>
 46. Pang F, Jiang YT, Zhang YQ, He MY, Ge JP (2015) Synergetic enhancement of photocatalytic activity with a photonic crystal film as a catalyst support. *J Mater Chem A* 3:21439–21443. <https://doi.org/10.1039/c5ta05224f>
 47. Li P, Wang Y, Wang AJ, Chen SL (2017) TiO_2 activity enhancement through synergistic effect of photons localization of photonic crystals and the sensitization of CdS quantum dots. *Photonics Nanostruct Fundam Appl* 23:12–20. <https://doi.org/10.1016/j.photonics.2016.11.006>
 48. Li P, Wang Y, Chen SL, Wang AJ (2015) Enhancement of gas–solid photocatalytic activity of nanocrystalline TiO_2 by SiO_2 opal photonic crystal. *J Mater Sci* 51:2079–2089. <https://doi.org/10.1007/s10853-015-9518-7>
 49. Zhang RF, Zeng F, Pang F, Ge JP (2018) Substantial enhancement toward the photocatalytic activity of CdS quantum dots by photonic crystal-supporting films. *ACS Appl Mater Interfaces* 10:42241–42248. <https://doi.org/10.1021/acsami.8b14437>
 50. Zhou J, Yang Y, Zhang CY (2013) A low-temperature solid-phase method to synthesize highly fluorescent carbon nitride dots with tunable emission. *Chem Commun* 49:8605–8607. <https://doi.org/10.1039/c3cc42266f>
 51. Zhang JA, Wang MZ, Ge XW, Wu MY, Wu QY, Yang JJ, Wang MY, Jin ZL et al. (2011) Facile fabrication of free-standing colloidal-crystal films by interfacial self-assembly. *J Colloid Interface Sci* 353:16–21. <https://doi.org/10.1016/j.jcis.2010.09.007>
 52. Lv JL, Dai K, Zhang JF, Geng L, Liang CH, Liu QC, Zhu GP, Chen C (2015) Facile synthesis of Z-scheme graphitic- $\text{C}_3\text{N}_4/\text{Bi}_2\text{MoO}_6$ nanocomposite for enhanced visible photocatalytic properties. *Appl Surf Sci* 358:377–384. <https://doi.org/10.1016/j.apsusc.2015.06.183>
 53. Zheng JH, Zhang L (2018) Incorporation of CoO nanoparticles in 3D marigold flower-like hierarchical architecture MnCo_2O_4 for highly boosting solar light photo-oxidation and reduction ability. *Appl Catal B Environ* 237:1–8. <https://doi.org/10.1016/j.apcatb.2018.05.060>

54. Park M, Seo JH, Kim JH, Park G, Park JY, Seo WS, Song H, Nam KM (2018) Effective formation of WO_3 nanoparticle/ Bi_2S_3 nanowire composite for improved photoelectrochemical performance. *J Phys Chem C* 122:17676–17685. <https://doi.org/10.1021/acs.jpcc.8b05555>
55. Yan T, Yan Q, Wang XD, Liu HY, Li MM, Lu SX, Xu WG, Sun M (2015) Facile fabrication of heterostructured g- $\text{C}_3\text{N}_4/\text{Bi}_2\text{MoO}_6$ microspheres with highly efficient activity under visible light irradiation. *Dalton Trans* 44:1601–1611. <https://doi.org/10.1039/c4dt02127d>
56. Zhao RY, Sun XX, Jin YR, Han JS, Wang L, Liu FS (2019) Au/Pd/g- C_3N_4 nanocomposites for photocatalytic degradation of tetracycline hydrochloride. *J Mater Sci* 54:5445–5456. <https://doi.org/10.1007/s10853-018-03278-7>
57. Rehman R, Lahiri SK, Islam A, Wei P, Xu Y (2021) Self-assembled hierarchical $\text{Cu}_2\text{O}@C_{18}\text{H}_{36}\text{O}_2$ nanoflakes for superior fenton-like catalysis over a wide range of pH. *ACS Omega* 6:22188–22201. <https://doi.org/10.1021/acsomega.1c02881>
58. Oyetade OA, Nyamori VO, Martincigh BS, Jonnalagadda SB (2015) Effectiveness of carbon nanotube–cobalt ferrite nanocomposites for the adsorption of rhodamine B from aqueous solutions. *RSC Adv* 5:22724–22739. <https://doi.org/10.1039/c4ra15446k>
59. Zhang YF, Selvaraj R, Sillanpaa M, Kim Y, Tai CW (2014) The influence of operating parameters on heterogeneous photocatalytic mineralization of phenol over BiPO_4 . *Chem Eng J* 245:117–123. <https://doi.org/10.1016/j.cej.2014.02.028>
60. Akhavan O, Abdolhad M, Esfandiar A, Mohatashamifar M (2010) Photodegradation of graphene oxide sheets by TiO_2 nanoparticles after a photocatalytic. *Reduct J Phys Chem C* 114:12955–12959. <https://doi.org/10.1021/jp103472c29>
61. Akhavan O (2010) Graphene nanomesh by ZnO nanorod photocatalysts. *ACS Nano* 4:4174–4180. <https://doi.org/10.1021/nn10074>
62. Miao YC, Yin HB, Peng L, Huo YN, Li HX (2016) $\text{BiOBr}/\text{Bi}_2\text{MoO}_6$ composite in flower-like microspheres with enhanced photocatalytic activity under visible-light irradiation. *RSC Adv* 6:13498–13504. <https://doi.org/10.1039/c5ra18987j>

Publisher's note Springer Nature remains neutral with regard to jurisdictional claims in published maps and institutional affiliations.

Springer Nature or its licensor (e.g. a society or other partner) holds exclusive rights to this article under a publishing agreement with the author(s) or other rightsholder(s); author self-archiving of the accepted manuscript version of this article is solely governed by the terms of such publishing agreement and applicable law.